

A staggered discontinuous Galerkin method for the simulation of Rayleigh waves

Eric T. Chung^{*}; Chi Yeung Lam^{*}; Jianliang Qian[†]

**Department of Mathematics*

The Chinese University of Hong Kong, Hong Kong SAR. Email: tschung@math.cuhk.edu.hk,

cylam@math.cuhk.edu.hk

†Department of Mathematics, Michigan State University, East Lansing, MI 48824. Email:

qian@math.msu.edu

(August 28, 2014)

Running head: **SDG method for Rayleigh waves**

ABSTRACT

Accurate simulation of Rayleigh waves is of critical importance in a variety of geophysical applications, such as exploration geophysics, geotechnical characterization, and earthquake-related damage assessment. Based on recent works on staggered discontinuous Galerkin methods, we propose for the simulation of Rayleigh waves a new method which enjoys energy conservation and extremely low grid dispersion, so that it naturally provides accurate long-time/long-range wave propagation. Moreover, it can handle with ease irregular surface topography and discontinuities in the subsurface models as it is a Galerkin-type method. Since it combines the advantages of both the staggered-grid finite difference method and the discontinuous Galerkin method, the proposed method offers a powerful tool for modeling Rayleigh waves and seismic waves in general.

INTRODUCTION

Accurate simulation of Rayleigh waves is of critical importance in a variety of geophysical applications, such as exploration geophysics, geotechnical characterization, and earthquake-related damage assessment (Aki and Richards, 2002). Consequently, it is a long-studied topic in geophysics in that many challenging problems arise in designing for Rayleigh wave simulation an accurate method which ideally should enjoy low grid dispersion, provide accurate long-time/long-range wave propagation, and allow irregular surface topography and discontinuities in the subsurface model. Based on recent works in Chung and Engquist (2006, 2009), we design a staggered discontinuous Galerkin method to tackle exactly these challenges: the new method enjoys extremely low grid dispersion as shown in Chung et al. (2013a) and Chan et al. (2013); it enjoys the energy-conservation property (Chung and Engquist, 2006, 2009) so that it naturally provides accurate long-time/long-range wave propagation; it can handle with ease irregular surface topography and discontinuities in the subsurface models as it is a Galerkin-type method.

In the literature, simulations of Rayleigh waves have been mainly tackled with finite-difference methods (FDM) and finite-element methods (FEM). In terms of FDM for Rayleigh waves, most of these methods are based on staggered-grid FDMs proposed by Madariaga (1976), Virieux (1986) and Levander (1988). When the surface topography is flat, the free-surface boundary condition associated with Rayleigh waves is relatively easy to handle in a staggered-grid FDM. In Bohlen and Saenger (2006), the staggered-grid and the rotated staggered-grid FDMs are applied to simulate Rayleigh waves with flat surface topography, and accuracy for both methods are carefully studied. It is well-known that one needs more points per wavelength for surface waves than body waves since

the surface wave in the case of flat topography mainly travels horizontally and decays exponentially in the vertical direction. To overcome this increase in the number of unknowns near the surface, Kosloff and Carcione (2010) proposes a variable-grid-spacing method in which the spatial grid is finer near the surface and coarser far away from the surface and the staggered sine and cosine transforms are applied to compute spatial derivatives; the resulting method is highly accurate and is able to handle propagation of Rayleigh waves at large offsets.

When the surface topography is non-flat, two remedies are proposed to treat free-surface boundary conditions in the setting of a staggered-grid FDM: one remedy using staircase approximation to the non-flat free surface topography, the other matching the free surface topography by deforming computational grids. In terms of using staircase approximation to the non-flat free surface topography, Levander (1988) originally proposed the stress-image technique to update the velocities for grid nodes on (flat) free surfaces, and Robertsson (1996) proposed an extension of this method, in which the grid nodes are classified into seven categories with different update rules. The vacuum formulation (Zahradnik et al., 1993) is developed along the same line by setting parameters to zero above the free surface so that surface topography can be implemented in the same manner as an internal material interface. However, numerical tests have shown that the simple vacuum formulation becomes unstable when using fourth-order or higher order spatial difference operators (Graves, 1996); consequently, Zeng et al. (2012) proposed an improved vacuum formulation to incorporate surface topography, in which the parameters at the surface grid nodes are averaged using the same scheme as for the interior grid nodes; this method is shown to be stable using fourth-order spatial difference operators without notable numerical dispersion. On the other hand, various methods are proposed to deform computational grids to match the free surface topography

by using curvilinear coordinates: Hestholm and Ruud (2002); Zhang and Chen (2006); Lombard et al. (2008) in the setting of a staggered-grid FDM and Appelö and Petersson (2009) in the setting of a non-staggered-grid FDM. Since these methods involve computation of spatial derivatives in the curved grid and application of the chain rule to calculate the required cartesian spatial derivatives, Komatitsch et al. (1996) proposed a method to solve the equation directly on curved grids.

Despite the efficiency of FDMs on structured grids, implementing free-surface conditions in FDMs can be difficult on an irregular domain. Therefore, Moczo et al. (1997) presented a hybrid method in which low-order FEMs were used near boundaries while second-order FDMs were used for the rest of the model, and Ma et al. (2004) presented another hybrid method which combined low-order FEMs with a fourth-order velocity-stress staggered-grid FDM. There are certainly plenty of advantages in using FEMs for surface topography since they allow the use of triangular meshes suitable for irregular surfaces. In terms of new developments in FEM for seismic wave modeling, several different methods are popular in geophysical community as briefly summarized in Basabe and Sen (2009): the spectral-element method, the mixed finite-element method, and the discontinuous Galerkin method. The spectral element method (SEM) is a class of high-order continuous Galerkin FEMs and originally developed for fluid dynamics (Patera, 1984), and it has been successfully applied to acoustic and elastic wave propagations (Seriani and Priolo, 1994; Komatitsch and Vilotte, 1998; Komatitsch et al., 2008). There are at least two major limitations associated with SEM. One limitation is the exclusive use of hexahedral meshes, which makes the design of an optimal mesh cumbersome in contrast to the flexibility offered by tetrahedral meshes; the other is the exclusive use of the classical explicit second-order Newmark scheme in the time integration (Hughes, 1987), which may cause some potential deterioration in accuracy if long-time simulation

is needed over many wavelengths. These two major limitations can be overcome by another class of FEMs: the discontinuous Galerkin (DG) FEM (Basabe and Sen, 2009) in combination with explicit time-marching Runge-Kutta methods (Cockburn and Shu, 1991; Cockburn et al., 2005) or the Lax-Wendroff time integration (Dumbser and Kaser, 2006). Raviart and Thomas (1977) introduced the mixed FEM that is suitable for the spatial approximation of the wave equation in the velocity-stress form, and Geveci (1988) analyzed its convergence. The advantage of using mixed formulations is that the energy is conserved both locally and globally, which is an important property described by wave equations. However, when a time discretization is applied, this method usually produces an implicit time-marching scheme because nondiagonal mass matrices may arise in the process, which make the time-stepping inefficient. The mass-lumping technique, which is a way to approximate the mass matrix by a diagonal matrix, is developed to improve the efficiency (Becache et al., 2000; Cohen et al., 2001). Various DG FEMs are briefly summarized in Basabe and Sen (2009), and these methods can be upwind flux-based or interior-penalty based so that they have different convergence properties.

According to the above literature survey, it seems that both the staggered-grid FDM (which is efficient in time-stepping and inefficient for irregular surfaces) and the DG FEM (which is efficient for irregular surfaces and inefficient in time-stepping) are powerful for seismic wave modeling. So the question is that: can we design a method which combines good features of both staggered-grid FDMs and DG FEMs? The staggered DG (SDG) method is exactly such an attempt. The SDG method has been successfully developed for many wave propagation problems (Chung and Engquist, 2006, 2009; Chung et al., 2013a; Chung and Ciarlet, 2013; Chung and Lee, 2012; Chan et al., 2013) and other applications (Chung et al., 2013b; Kim et al., 2013; Chung and Kim, 2014; Chung et al.,

2014a; Kim et al., 2014; Chung et al., 2014b). In terms of velocity-stress formulation for elastic waves, the SDG method starts with two sets of irregular, staggered grids, one for velocity and one for stress; furthermore, it designs two finite-element spaces on those two sets of staggered grids and carries out integration-by-parts to derive corresponding weak formulations; finally, it applies the standard leap-frog scheme for explicit time stepping. The SDG method enjoys several distinctive features that are particularly attractive: first, it conserves the wave energy automatically; second, it is optimally convergent in both L^2 -norm and energy norm; third, it yields block-diagonal mass matrices so that very efficient explicit time-stepping is allowed; fourth, it is flexible in handling complex geometries so that free surface conditions on nonflat surfaces can be imposed easily; fifth, as shown in Chung et al. (2013a) and Chan et al. (2013), it yields solutions with extremely low dispersion errors in that the order of dispersion error in terms of grid-size for the SDG method is two order higher than that of classical finite-difference methods based on non-staggered grids. Hence, the SDG method provides a competitive alternative for simulations of Rayleigh waves with irregular surface topography.

PROBLEM SETTINGS

The simulation of Rayleigh waves is mathematically modeled by a half-space problem. To simplify the presentation, we will consider the 2-D problems only. First, the domain of interest is the infinite half-space defined by

$$\widehat{\Omega} := \{(x, z) \mid -\infty < x < \infty, \Gamma(x) < z < \infty\}$$

where $\Gamma(x)$ is a function which models the surface topography. In the domain $\widehat{\Omega}$, we solve the following elastic wave equation

$$\rho \frac{\partial u}{\partial t} - \operatorname{div} \sigma = f, \quad (1)$$

$$A \frac{\partial \sigma}{\partial t} - \varepsilon(u) = 0, \quad (2)$$

where ρ is the density, $u = (u_1, u_2)^T$ is the velocity field and $\sigma = (\sigma_{ij})$ is the 2×2 symmetric stress tensor. In addition, $f = (f_1, f_2)^T$ is a given source term. We write $\sigma_1 = (\sigma_{11}, \sigma_{12})$ and $\sigma_2 = (\sigma_{21}, \sigma_{22})$ as the first and the second row of σ , respectively. The above divergence is defined as $\operatorname{div} \sigma = (\operatorname{div} \sigma_1, \operatorname{div} \sigma_2)^T$. Moreover, we have $\varepsilon(u)_{ij} = \frac{1}{2}(\partial_i u_j + \partial_j u_i)$. The matrix A is defined by

$$A = \begin{pmatrix} \lambda + 2\mu & \lambda & 0 & 0 \\ \lambda & \lambda + 2\mu & 0 & 0 \\ 0 & 0 & 2\mu & 0 \\ 0 & 0 & 0 & 2\mu \end{pmatrix}^{-1}$$

where we assume that $\sigma = (\sigma_{11}, \sigma_{22}, \sigma_{12}, \sigma_{21})^T$ in equation 2; λ and μ are the first and second Lamé parameters of the material. Introducing a skew-symmetric 2×2 matrix γ , we have

$$\rho \frac{\partial u}{\partial t} - \operatorname{div} \sigma = f, \quad (3)$$

$$A \frac{\partial \sigma}{\partial t} - \nabla u + \gamma = 0, \quad (4)$$

where

$$\gamma_{ij} = \frac{1}{2}(\partial_j u_i - \partial_i u_j).$$

Note that in the 2-D setting, the skew-symmetric matrix γ is equivalent to a scalar function. We remark that the role of γ in the SDG method is a Lagrange multiplier to enforce the symmetry of

the approximate stress tensor. The details will be explained in the next section. To solve the above elastic wave equation, we impose suitable initial conditions and the following free-surface boundary condition

$$\sigma n = 0 \quad \text{on } z = \Gamma(x)$$

where n is the outward normal to the free surface, and σn is the standard matrix-vector product.

We introduce some notations that will be used throughout the paper. For two tensors σ and α , we define

$$\sigma \cdot \alpha = \sum_{i=1}^2 \sum_{j=1}^2 \sigma_{ij} \alpha_{ij}.$$

For a tensor σ and a vector u , we define

$$\sigma \cdot \nabla u = \sum_{i=1}^2 \sigma_i \cdot \nabla u_i$$

and

$$u \cdot (\text{div } \sigma) = \sum_{i=1}^2 u_i (\text{div } \sigma_i).$$

For a unit vector n , we define

$$u \cdot (\sigma n) = \sum_{i=1}^2 u_i (\sigma_i \cdot n).$$

THE SDG METHOD

A staggered triangular grid

We will now present the triangulation of the domain by an unstructured staggered grid. Let Ω be the computational domain, which is a truncation of the infinite half-space $\widehat{\Omega}$ and is defined by

$$\Omega = \{(x, z) \mid -R < x < R, \Gamma(x) < z < L\}.$$

We assume that Ω is triangulated by an initial triangular mesh, called \mathcal{T}'_h . This mesh can be formed by any mesh generator. For each triangle in this mesh, we choose an interior point ν , and then subdivide each triangle into 3 sub-triangles by connecting this point ν to the three vertices of the triangle. A new mesh, called \mathcal{T}_h , is then formed by this sub-division process. That is, \mathcal{T}_h is the refined triangulation of \mathcal{T}'_h defined by the above construction. The set of all these nodes ν is denoted by \mathcal{N} . An example of such construction is illustrated in Figure 1. The triangles of the initial triangulation \mathcal{T}'_h are denoted by solid lines. An interior point is chosen for each initial triangle, and we divide the triangle into 3 sub-triangles. The newly formed edges are denoted by dotted lines.

Next, we define two types of macro elements. The first type of macro elements is defined with respect to the initial mesh. In particular, the triangles of the initial mesh \mathcal{T}'_h are called the first-type macro elements. We use $\mathcal{S}(\nu)$ to denote such a macro element, and we remark that these elements are parametrized by ν . An example of such an element is illustrated in Figure 2. The second type of macro elements is defined with respect to the edges of the initial triangulation \mathcal{T}'_h , and we use $\mathcal{R}(\kappa)$ to denote such a macro element. The macro element $\mathcal{R}(\kappa)$ is defined as the union of the two triangles in \mathcal{T}_h sharing the edge κ . An example of such an element is illustrated in Figure 3. If an edge κ of the initial triangulation lies on the boundary of the computational domain, then we define $\mathcal{R}(\kappa)$ to be the only triangle in \mathcal{T}_h having the edge κ . Moreover, we use the notation \mathcal{F}_u to represent the set of edges of the initial triangulation and \mathcal{F}_u^0 the subset of interior edges, as u will be defined to be continuous across those edges. We use the notation \mathcal{F}_σ to denote the set of new edges formed by the above sub-division process, as the normal components of σ will be defined to be continuous across those new edges. In Figure 1, edges in \mathcal{F}_u are represented by solid lines and

edges in \mathcal{F}_σ are represented by dotted lines.

Let $m \geq 1$ be a non-negative integer representing the order of polynomials used in our approximation space. For any triangle τ in the triangulation \mathcal{T}_h , we let $P^m(\tau)$ be the space of polynomials of degree at most m defined on τ . We define P^m as the space of piecewise $P^m(\tau)$ functions; that is, $v \in P^m$ if the restriction of v on each triangle $\tau \in \mathcal{T}_h$ is in $P^m(\tau)$. We remark that we do not impose any continuity of functions in P_m on the edges of the triangulation \mathcal{T}_h .

Next, we present definitions of the approximation spaces. First, we introduce the function space $(U_h)^2$ for the approximation of the velocity vector u . Each component of u belongs to the space U_h , which is defined by

$$U_h = \{v \in P^m \mid v \text{ is continuous on } \mathcal{F}_u^0\}. \quad (5)$$

Thus, the functions in the space U_h are polynomials of degree at most m on each triangle $\tau \in \mathcal{T}_h$ such that they are continuous across the internal edges of the initial triangulation \mathcal{T}'_h , namely, the set \mathcal{F}_u^0 . Since the functions in U_h are in general discontinuous on \mathcal{F}_σ , these functions are supported on $\mathcal{R}(\kappa)$, the second-type macro element. Second, we introduce the function space $(W_h)^2$ for the approximation of σ . Both of the vectors σ_1 and σ_2 belong to the space W_h , which is defined by

$$W_h = \{\alpha \in (P^m)^2 \mid \alpha \cdot n \text{ is continuous on } \mathcal{F}_\sigma\}. \quad (6)$$

The vector fields in the space W_h are polynomials of degree at most m on each triangle $\tau \in \mathcal{T}_h$ such that the normal components on the set of edges \mathcal{F}_σ are continuous. Since the vector fields in W_h are in general discontinuous on \mathcal{F}_u^0 , these vectors are supported on $\mathcal{S}(\nu)$, the first-type macro element. Finally, we introduce the function space X_h for the approximation of the function γ . We will take $X_h = P^{m-1}$, which contains functions that are discontinuous on all edges in the triangulation \mathcal{T}_h .

Derivation

We will now derive the SDG method for the approximation of equations 3 and 4. We consider the first component of equation 3, namely,

$$\rho \frac{\partial u_1}{\partial t} - \operatorname{div} \sigma_1 = f_1. \quad (7)$$

Let v_1 be a smooth test function. Multiplying equation 7 by the test function v_1 and integrating on $\mathcal{R}(\kappa)$ yields

$$\int_{\mathcal{R}(\kappa)} \rho \frac{\partial u_1}{\partial t} v_1 \, dx - \int_{\mathcal{R}(\kappa)} (\operatorname{div} \sigma_1) v_1 \, dx = \int_{\mathcal{R}(\kappa)} f_1 v_1 \, dx. \quad (8)$$

Using integration by parts, we have

$$\int_{\mathcal{R}(\kappa)} \rho \frac{\partial u_1}{\partial t} v_1 \, dx + \int_{\mathcal{R}(\kappa)} \sigma_1 \cdot \nabla v_1 \, dx - \int_{\partial \mathcal{R}(\kappa)} (\sigma_1 \cdot n) v_1 \, ds = \int_{\mathcal{R}(\kappa)} f_1 v_1 \, dx. \quad (9)$$

Similarly, for the second component of equation 3, we have

$$\int_{\mathcal{R}(\kappa)} \rho \frac{\partial u_2}{\partial t} v_2 \, dx + \int_{\mathcal{R}(\kappa)} \sigma_2 \cdot \nabla v_2 \, dx - \int_{\partial \mathcal{R}(\kappa)} (\sigma_2 \cdot n) v_2 \, ds = \int_{\mathcal{R}(\kappa)} f_2 v_2 \, dx. \quad (10)$$

Combining the above equations 9 and 10, we have

$$\int_{\mathcal{R}(\kappa)} \rho \frac{\partial u}{\partial t} \cdot v \, dx + \int_{\mathcal{R}(\kappa)} \sigma \cdot \nabla v \, dx - \int_{\partial \mathcal{R}(\kappa)} (\sigma n) \cdot v \, ds = \int_{\mathcal{R}(\kappa)} f \cdot v \, dx \quad (11)$$

for all smooth test functions $v = (v_1, v_2)^T$. We remark that equation 11 holds for all macro elements $\mathcal{R}(\kappa)$ and all test functions v such that $v = 0$ on the boundary of the computational domain Ω .

Next we consider equation 4. Let $\alpha = (\alpha_1, \alpha_2)^T$ be a smooth 2×2 test tensor, where α_1 and α_2 are two row vectors. Notice that α is not necessarily symmetric. Multiplying equation 4 by α and integrating on the macro element $\mathcal{S}(\nu)$, we have

$$\int_{\mathcal{S}(\nu)} A \frac{\partial \sigma}{\partial t} \cdot \alpha \, dx - \int_{\mathcal{S}(\nu)} \nabla u \cdot \alpha \, dx + \int_{\mathcal{S}(\nu)} \gamma \cdot \alpha \, dx = 0. \quad (12)$$

For the gradient term involving α_1 , we apply integration by parts to get

$$\int_{\mathcal{S}(\nu)} \nabla u_1 \cdot \alpha_1 \, dx = - \int_{\mathcal{S}(\nu)} u_1 \operatorname{div} \alpha_1 \, dx + \int_{\partial \mathcal{S}(\nu)} u_1 (\alpha_1 \cdot n) \, ds. \quad (13)$$

Similarly, for the gradient term involving α_2 , we have

$$\int_{\mathcal{S}(\nu)} \nabla u_2 \cdot \alpha_2 \, dx = - \int_{\mathcal{S}(\nu)} u_2 \operatorname{div} \alpha_2 \, dx + \int_{\partial \mathcal{S}(\nu)} u_2 (\alpha_2 \cdot n) \, ds. \quad (14)$$

Hence, using equations 13 and 14, we have

$$\int_{\mathcal{S}(\nu)} A \frac{\partial \sigma}{\partial t} \cdot \alpha \, dx + \int_{\mathcal{S}(\nu)} u \operatorname{div} \alpha \, dx - \int_{\partial \mathcal{S}(\nu)} u \cdot (\alpha n) \, ds + \int_{\mathcal{S}(\nu)} \gamma \cdot \alpha \, dx = 0. \quad (15)$$

Now, we will present the definition of the SDG method. The approximations of u , σ and γ are denoted by u_h , σ_h and γ_h and are obtained in the spaces $(U_h)^2$, $(W_h)^2$ and X_h , respectively. For any macro element $\mathcal{R}(\kappa)$, equation 11 suggests the following approximation

$$\int_{\mathcal{R}(\kappa)} \rho \frac{\partial u_h}{\partial t} \cdot v \, dx + \int_{\mathcal{R}(\kappa)} \sigma_h \cdot \nabla v \, dx - \int_{\partial \mathcal{R}(\kappa)} (\sigma_h n) \cdot v \, ds = \int_{\mathcal{R}(\kappa)} f \cdot v \, dx, \quad (16)$$

for any test function v in the space $(U_h)^2$. Summing over all $\mathcal{R}(\kappa)$, we have

$$\int_{\Omega} \rho \frac{\partial u_h}{\partial t} \cdot v \, dx + \sum_{\kappa \in \mathcal{F}_u} \left(\int_{\mathcal{R}(\kappa)} \sigma_h \cdot \nabla v \, dx - \int_{\partial \mathcal{R}(\kappa)} (\sigma_h n) \cdot v \, ds \right) = \int_{\Omega} f \cdot v \, dx, \quad \forall v \in (U_h)^2. \quad (17)$$

For any macro element $\mathcal{S}(\nu)$, equation 15 suggests the following approximation

$$\int_{\mathcal{S}(\nu)} A \frac{\partial \sigma_h}{\partial t} \cdot \alpha \, dx + \int_{\mathcal{S}(\nu)} u_h \operatorname{div} \alpha \, dx - \int_{\partial \mathcal{S}(\nu)} u_h \cdot (\alpha n) \, ds + \int_{\mathcal{S}(\nu)} \gamma_h \cdot \alpha \, dx = 0, \quad (18)$$

for any test function α in the space $(W_h)^2$. Summing over all $\mathcal{S}(\nu)$, we have

$$\int_{\Omega} A \frac{\partial \sigma_h}{\partial t} \cdot \alpha \, dx + \sum_{\nu \in \mathcal{N}} \left(\int_{\mathcal{S}(\nu)} u_h \operatorname{div} \alpha \, dx - \int_{\partial \mathcal{S}(\nu)} u_h \cdot (\alpha n) \, ds \right) + \int_{\Omega} \gamma_h \cdot \alpha \, dx = 0, \quad \forall \alpha \in (W_h)^2. \quad (19)$$

In addition, we will impose the following weak symmetry condition for σ_h

$$\int_{\tau} \sigma_h \cdot \eta \, dx = 0, \quad \forall \eta \in P^{m-1}(\tau), \quad \forall \tau \in \mathcal{T}_h. \quad (20)$$

Summing over all $\tau \in \mathcal{T}_h$, we have

$$\int_{\Omega} \sigma_h \cdot \eta \, dx = 0, \quad \forall \eta \in X_h. \quad (21)$$

Equations 17, 19 and 21 give the definition of our SDG method. Throughout the paper, we write

$u_h = (u_{h,1}, u_{h,2})^T$ and $\sigma_h = (\sigma_{h,1}, \sigma_{h,2})^T$, where $\sigma_{h,i}$ is the i -th row of σ_h .

Next, we will derive the linear system arising from equations 17, 19 and 21. Assume that the dimensions of U_h , W_h and X_h are m_U , m_W and m_X , respectively. Let $\{v^{(i)}\}_{i=1}^{m_U}$ be the basis functions of U_h , $\{\alpha^{(i)}\}_{i=1}^{m_W}$ be the basis functions of W_h , and $\{\eta^{(i)}\}_{i=1}^{m_X}$ be the basis functions of X_h .

Each component of u_h can be represented by

$$u_{h,k} = \sum_{i=1}^{m_U} u_{h,k}^{(i)} v^{(i)}, \quad k = 1, 2. \quad (22)$$

Moreover, each row of σ_h can be represented by

$$\sigma_{h,k} = \sum_{i=1}^{m_W} \sigma_{h,k}^{(i)} \alpha^{(i)}, \quad k = 1, 2. \quad (23)$$

Similarly, γ_h can be represented by

$$\gamma_h = \sum_{i=1}^{m_X} \gamma_h^{(i)} \eta^{(i)}. \quad (24)$$

We define the $m_U \times m_U$ mass matrix M_u by

$$(M_u)_{ij} = \int_{\Omega} \rho v^{(i)} v^{(j)} \, dx. \quad (25)$$

Notice that the basis functions of $(W_h)^2$ have the form $\beta^{(i)} = (\alpha^{(i)}, 0)^T$ or $\beta^{(i)} = (0, \alpha^{(i)})^T$. Thus,

we define the $2m_W \times 2m_W$ mass matrix M_{σ} by

$$(M_{\sigma})_{ij} = \int_{\Omega} (A\beta^{(i)}) \cdot \beta^{(j)} \, dx. \quad (26)$$

We also define the $2m_W \times m_X$ matrix C_γ by

$$(C_\gamma)_{ij} = \int_{\Omega} \beta^{(i)} \cdot \eta^{(j)} dx. \quad (27)$$

Moreover, with $v^{(i)} \in U_h$ and $\alpha^{(j)} \in W_h$, we define the following $m_U \times m_W$ matrix B by

$$B_{ij} = \sum_{\kappa \in \mathcal{F}_u} \left(\int_{\mathcal{R}(\kappa)} \alpha^{(j)} \cdot \nabla v^{(i)} dx - \int_{\partial \mathcal{R}(\kappa)} (\alpha^{(j)} \cdot n) v^{(i)} ds \right) \quad (28)$$

and the following $m_W \times m_U$ matrix B^* by

$$B_{ji}^* = - \sum_{\nu \in \mathcal{N}} \left(\int_{\mathcal{S}(\nu)} v^{(i)} \operatorname{div} \alpha^{(j)} dx - \int_{\partial \mathcal{S}(\nu)} v^{(i)} (\alpha^{(j)} \cdot n) ds \right). \quad (29)$$

Finally, we define the following two $m_U \times 1$ vectors $F_k = (F_k^{(i)})$ by

$$F_k^{(i)} = \int_{\Omega} f_k v^{(i)} dx, \quad k = 1, 2. \quad (30)$$

Let $\vec{u}_1 = (u_{h,1}^{(i)})$ and $\vec{u}_2 = (u_{h,2}^{(i)})$ be vectors of coefficients giving the approximate solutions $u_{h,1}$ and $u_{h,2}$ in equation 22. Moreover, we let $\vec{\sigma}_1 = (\sigma_{h,1}^{(i)})$ and $\vec{\sigma}_2 = (\sigma_{h,2}^{(i)})$ be vectors of coefficients giving the approximate solutions $\sigma_{h,1}$ and $\sigma_{h,2}$ in equation 23. We write $\vec{\sigma} = (\vec{\sigma}_1, \vec{\sigma}_2)^T$. Finally, we let $\vec{\gamma} = (\gamma_h^{(i)})$ be the vector of coefficients giving the approximate solutions γ_h in equation 24.

Using these definitions, equation 17 can be written as

$$\frac{d}{dt} M_u \vec{u}_1 + B \vec{\sigma}_1 = F_1, \quad \frac{d}{dt} M_u \vec{u}_2 + B \vec{\sigma}_2 = F_2. \quad (31)$$

Moreover, equation 19 can be written as

$$\frac{d}{dt} (M_\sigma \vec{\sigma}) - \begin{pmatrix} B^* & 0 \\ 0 & B^* \end{pmatrix} \begin{pmatrix} \vec{u}_1 \\ \vec{u}_2 \end{pmatrix} + C_\gamma \vec{\gamma} = 0. \quad (32)$$

Finally, equation 21 can be written as

$$C_\gamma^T \vec{\sigma} = 0. \quad (33)$$

Equations 31, 32 and 33 define the linear system for the SDG method. We remark that matrix B^* is the transpose of the matrix B , which is proved in Chung and Engquist (2009).

Time discretization

For time discretization, we will apply the standard leap-frog scheme. The velocity field \vec{u} is computed at the times $t_n = n\Delta t$ while the stress tensors $\vec{\sigma}$ and $\vec{\gamma}$ are computed at $t_{n+\frac{1}{2}} = (n + \frac{1}{2})\Delta t$, where Δt is the time step size and n is a non-negative integer. We will use \vec{u}^n to denote the approximate value of \vec{u} at time t_n . Moreover, we will use $\vec{\sigma}^{n+\frac{1}{2}}$ and $\vec{\gamma}^{n+\frac{1}{2}}$ to denote the approximate values of $\vec{\sigma}$ and $\vec{\gamma}$ at time $t_{n+\frac{1}{2}}$, respectively.

For equation 31, we use the central difference approximation in time at $t_{n+\frac{1}{2}}$ to obtain the following approximation

$$M_u \frac{\vec{u}_1^{n+1} - \vec{u}_1^n}{\Delta t} + B\vec{\sigma}_1^{n+\frac{1}{2}} = F_1^{n+\frac{1}{2}}, \quad M_u \frac{\vec{u}_2^{n+1} - \vec{u}_2^n}{\Delta t} + B\vec{\sigma}_2^{n+\frac{1}{2}} = F_2^{n+\frac{1}{2}}. \quad (34)$$

On the other hand, we evaluate equations 32 and 33 at the time t_n and use the central difference approximation for the time derivative to obtain the following

$$M_\sigma \frac{\vec{\sigma}^{n+\frac{3}{2}} - \vec{\sigma}^{n+\frac{1}{2}}}{\Delta t} - \tilde{B}^* \vec{u}^{n+1} + C_\gamma \frac{\vec{\gamma}^{n+\frac{3}{2}} + \vec{\gamma}^{n+\frac{1}{2}}}{2} = 0 \quad (35)$$

$$C_\gamma^T \vec{\sigma}^{n+\frac{3}{2}} = 0$$

where

$$\tilde{B}^* = \begin{pmatrix} B^* & 0 \\ 0 & B^* \end{pmatrix}.$$

Equation 35 can be written as the following saddle point system

$$\frac{2}{\Delta t} M_\sigma \vec{\sigma}^{n+\frac{3}{2}} + C_\gamma \vec{\gamma}^{n+\frac{3}{2}} = \frac{2}{\Delta t} M_\sigma \vec{\sigma}^{n+\frac{1}{2}} - C_\gamma \vec{\gamma}^{n+\frac{1}{2}} + 2\tilde{B}^* \vec{u}^{n+1} := R^{n+\frac{1}{2}} \quad (36)$$

$$C_\gamma^T \vec{\sigma}^{n+\frac{3}{2}} = 0.$$

Equations 34 and 36 define the time-marching formula. In particular, for any given \bar{u}^n , $\bar{\sigma}^{n+\frac{1}{2}}$ and $\bar{\gamma}^{n+\frac{1}{2}}$, where $n = 0, 1, 2, \dots$, we can use equation 34 to obtain \bar{u}^{n+1} . Then using the newly obtained \bar{u}^{n+1} , and current values of $\bar{\sigma}^{n+\frac{1}{2}}$ and $\bar{\gamma}^{n+\frac{1}{2}}$, we can use equation 36 to obtain approximations $\bar{\sigma}^{n+\frac{3}{2}}$ and $\bar{\gamma}^{n+\frac{3}{2}}$.

Although equation 36 is a coupled system with respect to the unknowns $\bar{\sigma}^{n+\frac{3}{2}}$ and $\bar{\gamma}^{n+\frac{3}{2}}$, it can be solved in the following element-wise manner. Since the mass matrix M_σ and the matrix C_γ are block diagonal, namely,

$$M_\sigma = \begin{pmatrix} M_\sigma^{\mathcal{S}(\nu_1)} & & & \\ & M_\sigma^{\mathcal{S}(\nu_2)} & & \\ & & \ddots & \\ & & & M_\sigma^{\mathcal{S}(\nu_N)} \end{pmatrix} \text{ and } C_\gamma = \begin{pmatrix} C_\gamma^{\mathcal{S}(\nu_1)} & & & \\ & C_\gamma^{\mathcal{S}(\nu_2)} & & \\ & & \ddots & \\ & & & C_\gamma^{\mathcal{S}(\nu_N)} \end{pmatrix}$$

where N is the number of triangles in the initial triangulation \mathcal{T}'_h , $M_\sigma^{\mathcal{S}(\nu_i)}$ is the local mass matrix corresponding to the macro element $\mathcal{S}(\nu_i)$ and $C_\gamma^{\mathcal{S}(\nu_i)}$ is the restriction of C_γ to the components corresponding to the macro element $\mathcal{S}(\nu_i)$, equation 36 can be solved as

$$\begin{aligned} \frac{2}{\Delta t} M_\sigma^{\mathcal{S}(\nu_i)} \bar{\sigma}^{n+\frac{3}{2}} + C_\gamma^{\mathcal{S}(\nu_i)} \bar{\gamma}^{n+\frac{3}{2}} &= R^{n+\frac{1}{2}} \\ (C_\gamma^{\mathcal{S}(\nu_i)})^T \bar{\sigma}^{n+\frac{3}{2}} &= 0 \end{aligned} \tag{37}$$

where $\bar{\sigma}^{n+\frac{3}{2}}$, $\bar{\gamma}^{n+\frac{3}{2}}$ and $R^{n+\frac{1}{2}}$ are understood as the restriction to the components corresponding to the macro element $\mathcal{S}(\nu_i)$. Similarly, the mass matrix M_u is also block diagonal, namely,

$$M_u = \begin{pmatrix} M_u^{\mathcal{R}(\kappa_1)} & & & \\ & M_u^{\mathcal{R}(\kappa_2)} & & \\ & & \ddots & \\ & & & M_u^{\mathcal{R}(\kappa_F)} \end{pmatrix}$$

where F is the number of second type macro elements, which is the same as the number of edges in the initial triangulation \mathcal{T}'_h . Therefore, equation 34 can be solved element-by-element as well.

Numerical stability

We will now derive a sufficient condition on the size of Δt for the stability of the SDG method in equations 34 and 35. We will assume that the source term $f = 0$ to simplify the calculations, and we remark that the same steps can be used to show stability of the method when $f \neq 0$. First, multiplying equation 34 by $\bar{u}^{n+1} + \bar{u}^n$, we obtain for $k = 1, 2$,

$$\left(M_u \frac{\bar{u}_k^{n+1} - \bar{u}_k^n}{\Delta t}, \bar{u}_k^{n+1} + \bar{u}_k^n \right) + \left(B \bar{\sigma}_k^{n+\frac{1}{2}}, \bar{u}_k^{n+1} + \bar{u}_k^n \right) = \left(F_k^{n+\frac{1}{2}}, \bar{u}_k^{n+1} + \bar{u}_k^n \right). \quad (38)$$

Moreover, multiplying equation 35 by $\bar{\sigma}^{n+\frac{3}{2}} + \bar{\sigma}^{n+\frac{1}{2}}$, we obtain

$$\left(M_\sigma \frac{\bar{\sigma}^{n+\frac{3}{2}} - \bar{\sigma}^{n+\frac{1}{2}}}{\Delta t}, \bar{\sigma}^{n+\frac{3}{2}} + \bar{\sigma}^{n+\frac{1}{2}} \right) - \left(\tilde{B}^* \bar{u}^{n+1}, \bar{\sigma}^{n+\frac{3}{2}} + \bar{\sigma}^{n+\frac{1}{2}} \right) = 0 \quad (39)$$

By the fact that $B^* = B^T$ which is proved in Chung and Engquist (2009) and the definition of \tilde{B}^* , we have

$$\begin{aligned} & \left(B \bar{\sigma}_1^{n+\frac{1}{2}}, \bar{u}_1^n \right) + \left(B \bar{\sigma}_2^{n+\frac{1}{2}}, \bar{u}_2^n \right) - \left(\tilde{B}^* \bar{u}^n, \bar{\sigma}^{n+\frac{1}{2}} \right) \\ &= \left(\bar{\sigma}_1^{n+\frac{1}{2}}, B^T \bar{u}_1^n \right) + \left(\bar{\sigma}_2^{n+\frac{1}{2}}, B^T \bar{u}_2^n \right) - \left(\tilde{B}^* \bar{u}^n, \bar{\sigma}^{n+\frac{1}{2}} \right) \\ &= \left(\bar{\sigma}_1^{n+\frac{1}{2}}, B^* \bar{u}_1^n \right) + \left(\bar{\sigma}_2^{n+\frac{1}{2}}, B^* \bar{u}_2^n \right) - \left(\tilde{B}^* \bar{u}^n, \bar{\sigma}^{n+\frac{1}{2}} \right) \\ &= 0. \end{aligned} \quad (40)$$

Let $N > 1$ be a fixed integer. Summing equations 38 and 39 from $n = 0$ to $n = N - 1$ and using equation 40, we have

$$E^N = E^0 + \frac{\Delta t}{2} \left(\tilde{B} \bar{\sigma}^{N+\frac{1}{2}}, \bar{u}^N \right) - \frac{\Delta t}{2} \left(\bar{\sigma}^{\frac{1}{2}}, \tilde{B}^* u^0 \right), \quad (41)$$

where

$$E^n := \frac{1}{2} \left(\|\vec{u}_1^n\|_{M_u}^2 + \|\vec{u}_2^n\|_{M_u}^2 + \|\vec{\sigma}^{n+\frac{1}{2}}\|_{M_\sigma}^2 \right),$$

and the norms above are defined as

$$\|\vec{u}_k^n\|_{M_u}^2 = (M_u \vec{u}_k^n, \vec{u}_k^n), \quad k = 1, 2; \quad \|\vec{\sigma}^{n+\frac{1}{2}}\|_{M_\sigma}^2 = (M_\sigma \vec{\sigma}^{n+\frac{1}{2}}, \vec{\sigma}^{n+\frac{1}{2}}).$$

Let $K := \widetilde{M}_u^{-\frac{1}{2}} \widetilde{B} M_\sigma^{-\frac{1}{2}}$, where

$$\widetilde{M}_u = \begin{pmatrix} M_u & 0 \\ 0 & M_u \end{pmatrix}.$$

By the Cauchy-Schwarz inequality, we have

$$\left(\widetilde{B} \vec{\sigma}^{N+\frac{1}{2}}, \vec{u}^N \right) \leq \|K\|_2 \|\vec{u}^N\|_{\widetilde{M}_u} \|\vec{\sigma}^{N+\frac{1}{2}}\|_{M_\sigma}, \quad (42)$$

where

$$\|\vec{u}^N\|_{\widetilde{M}_u}^2 = \|\vec{u}_1^N\|_{M_u}^2 + \|\vec{u}_2^N\|_{M_u}^2.$$

We will now show that the SDG method is stable if $\Lambda := \Delta t \|K\|_2 < 2$. Using this assumption, equation 41 can be written as

$$E^N \leq E^0 + \Lambda \|\vec{u}^N\|_{\widetilde{M}_u} \|\vec{\sigma}^{N+\frac{1}{2}}\|_{M_\sigma} + \Lambda \|\vec{u}^0\|_{\widetilde{M}_u} \|\vec{\sigma}^{\frac{1}{2}}\|_{M_\sigma}$$

which becomes

$$E^N \leq E^0 + \frac{\Lambda}{2} \left(\|\vec{u}^N\|_{\widetilde{M}_u}^2 + \|\vec{\sigma}^{N+\frac{1}{2}}\|_{M_\sigma}^2 \right) + \frac{\Lambda}{2} \left(\|\vec{u}^0\|_{\widetilde{M}_u}^2 + \|\vec{\sigma}^{\frac{1}{2}}\|_{M_\sigma}^2 \right).$$

Hence, we have

$$E^N \leq \frac{1 + \frac{\Lambda}{2}}{1 - \frac{\Lambda}{2}} E^0.$$

The above inequality gives the stability of the SDG method since $\Lambda < 2$. To find the explicit form of $\|K\|_2$, it is known that $\|K\|_2$ is proportional to h^{-1} , where h is the mesh size. Thus we can write

$\|K\|_2 = Ch^{-1}$ for some constant C . The value of C can be found by computing $\|K\|_2$ for different values of h and by using a least-squares fitting.

Construction of basis functions

We will present the construction of basis functions in this section. First, we describe the basis functions for U_h . By definition, a function $v \in U_h$ is a polynomial of degree $m \geq 1$ on each triangle $\tau \in \mathcal{T}_h$ and is continuous on the edges $\kappa \in \mathcal{F}_u^0$. Thus, v is decoupled along the boundaries of the second-type macro elements $\mathcal{R}(\kappa)$ for all $\kappa \in \mathcal{F}_u$. Therefore, the basis functions for the space U_h are constructed locally on $\mathcal{R}(\kappa)$. We will consider an interior edge $\kappa \in \mathcal{F}_u^0$ and discuss the corresponding construction of basis functions on $\mathcal{R}(\kappa)$. The case that κ belongs to the boundary of the computational domain can be constructed in the same way. With reference to Figure 3, we will need piecewise polynomials of degree m that are continuous on κ . Thus, the basis functions can be taken as the standard conforming finite element basis functions applied to the domain $\mathcal{R}(\kappa)$ with a triangulation composed of two triangles. Secondly, for the space X_h , the basis functions can be taken as Lagrange basis functions on each triangle in \mathcal{T}_h , since there is no continuity requirement.

Finally, we describe the construction of the basis functions for the space W_h . By definition, a vector $\alpha \in W_h$ is a vector polynomial on each triangle $\tau \in \mathcal{T}_h$ with continuous normal components on the edges $\kappa \in \mathcal{F}_\sigma$. Thus, α is decoupled along the boundaries of the first-type macro elements $\mathcal{S}(\nu)$ for all $\nu \in \mathcal{N}$. Therefore, the basis functions for the space W_h are constructed locally on $\mathcal{S}(\nu)$. We will now present a convenient way to construct these functions. Consider a first-type macro element $\mathcal{S}(\nu)$. Let P_1, P_2, P_3 be the three vertices of $\mathcal{S}(\nu)$ and $P_4 = \nu$, which is the point chosen for the subdivision process required by the SDG method; see Figure 4. The corresponding three

sub-triangles are denoted by $\tau_1 = P_2P_3P_4$, $\tau_2 = P_1P_3P_4$ and $\tau_3 = P_1P_2P_4$. Moreover, for each of the three edges P_kP_4 , ($k = 1, 2, 3$), in the interior of $\mathcal{S}(\nu)$, we define a region ω_k by the union of the two sub-triangles having the edge P_kP_4 . That is, $\omega_1 = \tau_2 \cup \tau_3$, $\omega_2 = \tau_1 \cup \tau_3$ and $\omega_3 = \tau_1 \cup \tau_2$. In addition, we use n_k , $k = 1, 2, 3$, to denote a fixed unit normal vector for the edges P_kP_4 . The basis functions are divided into three types, and each of these three types of basis functions is supported in ω_1, ω_2 , and ω_3 , respectively. We will present the construction of basis function for the first type, namely those basis functions having support in ω_1 . The other two types can be constructed similarly. For the first type of basis functions α , we impose the following conditions

$$\alpha \cdot n_2 = 0, \text{ on } P_2P_4; \quad \alpha \cdot n_3 = 0, \text{ on } P_3P_4,$$

that is, α has zero normal component on the edges P_2P_4 and P_3P_4 . To obtain the above condition, we require $\alpha \cdot n_2$ to be identically zero on ω_2 and $\alpha \cdot n_3$ to be identically zero on ω_3 . Notice that, using this construction, we have $\alpha \cdot n_2$ and $\alpha \cdot n_3$ are identically zero on τ_1 , since τ_1 is the intersection of ω_2 and ω_3 . Next, we recall that the space W_h requires that $\alpha \cdot n_1$ be continuous on P_1P_4 . We now consider ω_1 and define $\alpha \cdot n_1$ to be a polynomial of degree m in each sub-triangle of ω_1 such that $\alpha \cdot n_1$ is continuous on P_1P_4 . Similar to the construction of basis functions for the space U_h , we now choose basis functions of $\alpha \cdot n_1$ on ω_1 to be the classical conforming finite element basis functions defined in the domain ω_1 corresponding to the triangulation $\omega_1 = \tau_2 \cup \tau_3$. The construction of basis function is now completed. Since both $\alpha \cdot n_1$ and $\alpha \cdot n_3$ are specified in τ_2 , the vector α in τ_2 can be re-constructed. Similarly, both $\alpha \cdot n_1$ and $\alpha \cdot n_2$ are specified in τ_3 so that the vector α can be

re-constructed. Specifically, we can then write

$$\alpha(x) \cdot n_1 = \begin{cases} g_2(x) & \text{in } \tau_2 \\ g_3(x) & \text{in } \tau_3 \end{cases}$$

where g_2 and g_3 are polynomials of degree m chosen in the way explained above. On τ_2 , we have $\alpha \cdot n_1 = g_2$ and $\alpha \cdot n_3 = 0$. Hence, we have on τ_2 ,

$$\alpha = \frac{g_2}{1 - (n_1 \cdot n_3)^2} n_1 - \frac{(n_1 \cdot n_3)g_2}{1 - (n_1 \cdot n_3)^2} n_3.$$

Similarly, we have on τ_3 ,

$$\alpha = \frac{g_3}{1 - (n_1 \cdot n_2)^2} n_1 - \frac{(n_1 \cdot n_2)g_3}{1 - (n_1 \cdot n_2)^2} n_2.$$

In Figure 5, plots of the first type of basis functions for the case $m = 1$ are shown. Notice that, these basis functions have support in ω_1 . Moreover, since $m = 1$, there are only 4 distinct basis functions. In particular, ω_1 is the union of two sub-triangles τ_2 and τ_3 . By the above construction, we need basis functions for $\alpha \cdot n_1$ that are linear in each of τ_2 and τ_3 , and are continuous on P_1P_4 . Thus, we see that there are only 4 choices, by taking $\alpha \cdot n_1$ equal to one at one of the four vertices of ω_1 and zero at the other three vertices.

NUMERICAL RESULTS

In this section, we present some numerical results to show the performance of the SDG method for the simulation of Rayleigh waves. For our test examples, the velocities and stresses are zero initially, and a point source is vertically excited near the free surface. The source function is taken

as the first derivative of a Gaussian function defined as

$$w(t) = 2\pi f(t - t_0)e^{-\pi^2 f^2 (t-t_0)^2}$$

where f is the frequency(Hz) and t_0 is a shift in time(s). In all the examples discussed below, the frequency f is 50 Hz and t_0 is 24ms.

We will perform computations in both rectangular and irregular domains. For rectangular domains, we first subdivide the domain into equal size squares, and then we divide each square into two triangles, which forms the initial mesh \mathcal{T}'_h . Then we choose the centroid as ν in each triangle and subdivide each triangle into three in the way presented in the previous section. The resulting triangulation is \mathcal{T}_h . The mesh size h for this case is the length of the diagonal of the square. For irregular domains, we first divide them into a rectangle and an irregular subdomain. In order to shorten the running time, the submesh on the rectangle domain is structured. In addition, the mesh on the irregular subdomain is constructed so that the surface topography is captured. The diameter of the triangles in the irregular subdomain is about the same size as the mesh size of the rectangle. In this case we define the mesh size h to be the length of the diagonal of the initial squares in the rectangle. In all the simulations, we will use $\Delta t \approx 2\sqrt{2}hC^{-1}$ which is sufficient for stability.

In our examples, we will use four different materials. Their P-wave velocity v_p , S-wave velocity v_s , density ρ , Poisson's ratio ν are listed in the following table:

We can compute the stability condition by using the method described in the previous section. For example, we obtain $C \approx 230$ and $C \approx 238$ for material 1 and material 2 respectively. Thus the stability condition for these two cases are $\Delta t < 8.7 \times 10^{-3}h$ and $\Delta t < 8.5 \times 10^{-3}h$ respectively.

Material	v_p (ms ⁻¹)	v_s (ms ⁻¹)	ρ (kg m ⁻³)	ν
1	520	300	1500	0.251
2	520	52	1500	0.495
3	160	50	1800	0.446
4	200	80	2000	0.405

In example 1, we simulate Rayleigh waves without PMLs. The domain of interest is $[40\text{m}, 240\text{m}] \times [0\text{m}, 100\text{m}]$ filled with Material 1. Our computational domain is large enough so that no reflection is created from the boundary of our domain of interest. The point source is vertically excited at $[100\text{m}, 0\text{m}]$. The mesh size $h = 0.2\text{m}$ and the time step size is 0.04ms . In Figure 6, we show a snapshot for the vertical velocity u_2 at $t = 0.25\text{s}$. From this figure we can clearly see that the Rayleigh waves are well captured. In Figure 7, we compare the accuracy of our solution with a reference solution computed by a fourth order finite difference scheme at various observation points. From these comparisons, we see that the SDG method is able to compute the correct solution. In Figure 8, we compute the relative rate of change of energy over time. The relative rate of change of energy is defined as

$$\delta(t) = \frac{1}{E_\infty} \frac{dE}{dt},$$

where the energy $E(t)$ is given by

$$E(t) = \frac{1}{2} \int_{\Omega} \left(\rho u_1^2 + \rho u_2^2 + \sigma^T A \sigma \right) dx.$$

and E_∞ is value of E at the end of simulation. After the initial disturbance due to the point source, the energy remains unchanged, which agrees with the energy conservation property of our scheme.

In example 2, we simulate Rayleigh waves for a model with high Poisson's ratio. The domain of interest is $[5\text{m}, 45\text{m}] \times [0\text{m}, 15\text{m}]$, which is filled with Material 2 and surrounded by multi-axial PMLs (see for example Meza-Fajardo and Papageorgiou (2008)) with 5m width. The point source is vertically excited at $[10\text{m}, 0\text{m}]$. The mesh size $h = 0.05\text{m}$ and the time step size is 0.01ms. Snapshots for u_2 at various times are shown in Figure 9, and we see clearly that the Rayleigh waves are well captured. In addition, we show the comparison of our solution to the reference solution at some observation points in Figure 10, and it is evident that our SDG method is able to produce accurate numerical solutions.

In example 3 and 4, we demonstrate the ability of our scheme to simulate Rayleigh waves in a domain with surface topography. The domains are filled with Material 2. In example 3, the surface topography is mathematically modelled by $\Gamma_3(x) = -4 \exp(-\frac{(x-8)^2}{20})$. The point source is vertically excited at $[8\text{m}, -4\text{m}]$. The mesh size $h = 0.05\text{m}$ and the time step size is $3.33\mu\text{s}$. The snapshots of u_2 at various times are shown in Figure 11. We clearly see that the Rayleigh waves are captured.

In example 4, the surface topography is modelled by $\Gamma_4(x) = 4 \exp(-\frac{(x-16)^2}{20})$. The point source is vertically excited at $[6\text{m}, 0\text{m}]$. The mesh size $h = 0.05\text{m}$ and the time step size is 0.006ms. The snapshots of u_2 at various times are shown in Figure 12. We also see that the Rayleigh waves are well captured.

In example 5, we incorporate internal discontinuities as well as the surface topology in our model. The surface topology is given by $\Gamma_4(x) = -4 \exp(-\frac{(x-8)^2}{20})$, which is the same as Γ_3 in example 3. The internal interface between the two layers of different materials is given by $\Gamma_4(x) + 8$. The

upper layer is filled with Material 3 and the lower layer is filled with Material 4. The mesh size is $h = 0.10\text{m}$ and the time step size is 0.0125 ms . The snapshots of the solution at various times are shown in Figure 13. We see that the surface waves are well captured. Moreover, the reflection and transmission of the waves at the internal discontinuities are accurately computed.

CONCLUSIONS

We developed a SDG method for the velocity-stress formulation of elastic waves with application to the simulations of Rayleigh waves. The method enjoys several distinctive features that are particularly attractive: first, it conserves the wave energy automatically; second, it is optimally convergent in both L^2 -norm and energy norm; third, it yields block-diagonal mass matrices so that very efficient explicit time-stepping is allowed; fourth, it is flexible in handling complex geometries so that free surface conditions on nonflat surfaces can be imposed easily; fifth, it yields solutions with extremely low dispersion errors. Numerical examples have shown that the SDG method provides a competitive alternative for simulations of Rayleigh waves with irregular surface topography.

ACKNOWLEDGEMENTS

The research of Eric Chung is partially supported by Hong Kong RGC General Research Fund (Project: 400411). The research of Jianliang Qian is partially supported by NSF.

REFERENCES

- Aki, K., and P. G. Richards, 2002, *Quantitative seismology*: University Science Books.
- Appelö, D., and N. A. Petersson, 2009, A stable finite difference method for the elastic wave equation on complex geometries with free surfaces: *Communications in Computational Physics*, **5**, 84–107.
- Basabe, J. D., and M. K. Sen, 2009, New developments in the finite-element method for seismic modeling: *The Leading Edge*, **28**, 562–567.
- Becache, E., P. Joly, and C. Tsogka, 2000, An analysis of new mixed finite elements for the approximation of wave propagation problems: *SIAM J. Numer. Anal.*, **37**, 1053–1084.
- Bohlen, T., and E. H. Saenger, 2006, Accuracy of heterogeneous staggered-grid finite-difference modeling of Rayleigh waves.: *Geophysics*, **71**, 109–115.
- Chan, H., E. Chung, and G. Cohen, 2013, Stability and dispersion analysis of staggered discontinuous Galerkin method for wave propagation.: *Int. J. Numer. Anal. Model.*, **10**, 233–256.
- Chung, E., and P. Ciarlet, 2013, A staggered discontinuous Galerkin method for wave propagation in media with dielectrics and meta-materials.: *J. Comput. Appl. Math.*, **239**, 189–207.
- Chung, E., P. Ciarlet, and T. Yu, 2013a, Convergence and superconvergence of staggered discontinuous Galerkin methods for the three-dimensional maxwell’s equations on cartesian grids.: *J. Comput. Phys.*, **235**, 14–31.
- Chung, E., B. Cockburn, and G. Fu, 2014a, The staggered DG method is the limit of a hybridizable DG method.: *SIAM J. Numer. Anal.*, **52**, 915–932.
- Chung, E., and B. Engquist, 2006, Optimal discontinuous Galerkin methods for wave propagation.: *SIAM J. Numer. Anal.*, **44**, 2131–2158.

- , 2009, Optimal discontinuous Galerkin methods for the acoustic wave equation in higher dimensions.: *SIAM J. Numer. Anal.*, **47**, 3820–3848.
- Chung, E., and H. Kim, 2014, A deluxe FETI-DP algorithm for a hybrid staggered discontinuous Galerkin method for H(curl)-elliptic problems.: *Internat. J. Numer. Methods Engrg*, **98**, 1–23.
- Chung, E., H. Kim, and O. Widlund, 2013b, Two-level overlapping schwarz algorithms for a staggered discontinuous Galerkin method.: *SIAM J. Numer. Anal.*, **51**, 47–67.
- Chung, E., and C. Lee, 2012, A staggered discontinuous Galerkin method for the curl-curl operator.: *IMA J. Numer. Anal.*, **32**, 1241–1265.
- Chung, E., M. Yuen, and L. Zhong, 2014b, A-posteriori error analysis for a staggered discontinuous Galerkin discretization of the time-harmonic Maxwell’s equations.: *Appl. Math, Comput.*, **237**, 613–631.
- Cockburn, B., J. Qian, F. Reitich, and J. Wang, 2005, An accurate spectral/discontinuous finite-element formulation of a phase-space-based level set approach to geometrical optics: *J. Comput. Phys.*, **208**, 75–195.
- Cockburn, B., and C.-W. Shu, 1991, The Runge-Kutta local projection P1-Discontinuous Galerkin finite element method for scalar conservation laws: *Mathematical Modelling and Numerical Analysis*, **25**, 337–361.
- Cohen, G., P. Joly, N. Tordjman, and J. Roberts, 2001, Higher order triangular finite elements with mass lumping for the wave equation: *SIAM J. Numer. Anal.*, **38**, 2047–2078.
- Dumbser, M., and M. Kaser, 2006, An arbitrary high-order discontinuous Galerkin method for elastic waves on unstructured meshes-II. The three-dimensional isotropic case: *Geophys. J. Internat.*, **167**, 319–336.

- Geveci, T., 1988, On the application of mixed finite element methods to the wave equation: *RAIRO Model. Math. Anal. Numer.*, **22**, 243–250.
- Graves, R. W., 1996, Simulating seismic wave propagation in 3d elastic media using staggered-grid finite differences: *Bulletin of the Seismological Society of America*, **86**, 1091–1106.
- Hestholm, S., and B. Ruud, 2002, 3d free-boundary conditions for coordinate-transform finite-difference seismic modelling: *Geophysical Prospecting*, **50**, 463–474.
- Hughes, T., 1987, *The finite element method. Linear static and dynamic finite element analysis*: Prentice-Hall International, Inc.
- Kim, H., E. Chung, and C. Lee, 2013, A staggered discontinuous Galerkin method for the Stokes system.: *SIAM J. Numer. Anal.*, **51**, 3327–3350.
- , 2014, A BDDC algorithm for a class of staggered discontinuous Galerkin methods.: *Comput. Math. Appl.*, **67**, 1373–1389.
- Komatitsch, D., F. Coutel, and P. Mora, 1996, Tensorial formulation of the wave equation for modelling curved interfaces: *Geophysical Journal International*, **127**, 156–168.
- Komatitsch, D., J. Labarta, and D. Michea, 2008, A simulation of seismic wave propagation at high resolution in the inner core of the Earth on 2166 processors of MareNostrum: *Lecture Notes in Computer Science*, **5336**, 364–377.
- Komatitsch, D., and J. P. Vilotte, 1998, The spectral-element method: an efficient tool to simulate the seismic response of 2D and 3D geological structures: *Bull. Seis. Soc. Am.*, **88**, 368–392.
- Kosloff, D., and J. M. Carcione, 2010, Two-dimensional simulation of Rayleigh waves with staggered sine/cosine transforms and variable grid spacing.: *Geophysics*, **75**, 133–140.
- Levander, A. R., 1988, Fourth-order finite-difference p-sv seismograms: *Geophysics*, **53**, 1425–1436.

- Lombard, B., J. Piraux, C. Gélis, and J. Virieux, 2008, Free and smooth boundaries in 2-d finite-difference schemes for transient elastic waves: *Geophysical Journal International*, **172**, 252–261.
- Ma, S., R. J. Archuleta, and P. Liu, 2004, Hybrid modeling of elastic p-sv wave motion: a combined finite-element and staggered-grid finite-difference approach: *Bulletin of the Seismological Society of America*, **94**, 1557–1563.
- Madariaga, R., 1976, Dynamics of an expanding circular fault: *Bull. Seis. Soc. Am.*, **66**, 639–666.
- Meza-Fajardo, K., and A. Papageorgiou, 2008, A nonconvolutional, split-field, perfectly matched layer for wave propagation in isotropic and anisotropic elastic media: stability analysis: *Bulletin of the Seismological Society of America*, **98**, 1811–1836.
- Moczo, P., E. Bystrický, J. Kristek, J. M. Carcione, and M. Bouchon, 1997, Hybrid modeling of p-sv seismic motion at inhomogeneous viscoelastic topographic structures: *Bulletin of the Seismological Society of America*, **87**, 1305–1323.
- Patera, A. T., 1984, A spectral element method for fluid dynamics: Laminar flow in a channel expansion: *J. Comput. Phys.*, **54**, 468–488.
- Raviart, P. A., and J. M. Thomas, 1977, A mixed finite element method for 2nd order problems: Presented at the *Mathematical Aspects of the Finite Element Method*, Lecture Notes in Math. 606, Springer-Verlag, Berlin, Heidelberg, New York.
- Robertsson, J. O., 1996, A numerical free-surface condition for elastic/viscoelastic finite-difference modeling in the presence of topography: *Geophysics*, **61**, 1921–1934.
- Seriani, G., and E. Priolo, 1994, Spectral element method for acoustic wave simulation in heterogeneous media: *Finite Element in Analysis and Design*, **16**, 337–348.
- Virieux, J., 1986, P-SV wave propagation in heterogeneous media: Velocity-stress finite-difference

- method: *Geophysics*, **51**, 889–901.
- Zahradnik, J., P. Moczo, and F. Hron, 1993, Testing four elastic finite-difference schemes for behavior at discontinuities: *Bulletin of the Seismological Society of America*, **83**, 107–129.
- Zeng, C., J. Xia, R. D. Miller, and G. P. Tsoflias, 2012, An improved vacuum formulation for 2D finite-difference modeling of Rayleigh waves including surface topography and internal discontinuities.: *Geophysics*, **77**, 1–9.
- Zhang, W., and X. Chen, 2006, Traction image method for irregular free surface boundaries in finite difference seismic wave simulation: *Geophysical Journal International*, **167**, 337–353.

LIST OF FIGURES

- 1 An example of the initial triangulation \mathcal{T}'_h (denoted by solid lines) and the subdivision of triangles of \mathcal{T}'_h by interior points (denoted by solid dots).
- 2 A first-type macro element $\mathcal{S}(\nu)$.
- 3 A second-type macro element $\mathcal{R}(\kappa)$.
- 4 Notations for the construction of basis for W_h .
- 5 Plots of the first-type basis functions for W_h on $\mathcal{S}(\nu)$ with $m = 1$.
- 6 The snapshot for the vertical velocity u_2 at $t = 0.25s$ in example 1.
- 7 Comparison of our solution (DG) to a fourth-order finite different scheme (FD) at various observation points in example 1.
- 8 The relative rate of change of the energy function $E(t)$ in example 1. Note that the green line, which represents the source function, is not related to the y axis in the figure.
- 9 Snapshots for the vertical velocity u_2 in example 2. The black lines indicate the interface between the domain of interest and the MPMLs.
- 10 Comparison of our solution (DG) to a fourth-order finite different scheme (FD) at various observation points in example 2.
- 11 Snapshots for the vertical velocity u_2 in example 3. The black lines indicate the interface between the domain of interest and the MPMLs.
- 12 Snapshots for the vertical velocity u_2 in example 4. The black lines indicate the interface between the domain of interest and the MPMLs.
- 13 Snapshots for the vertical velocity u_2 in example 5. The black lines indicate the interface between the domain of interest and the MPMLs. The dotted lines indicate the interface between

the two materials.

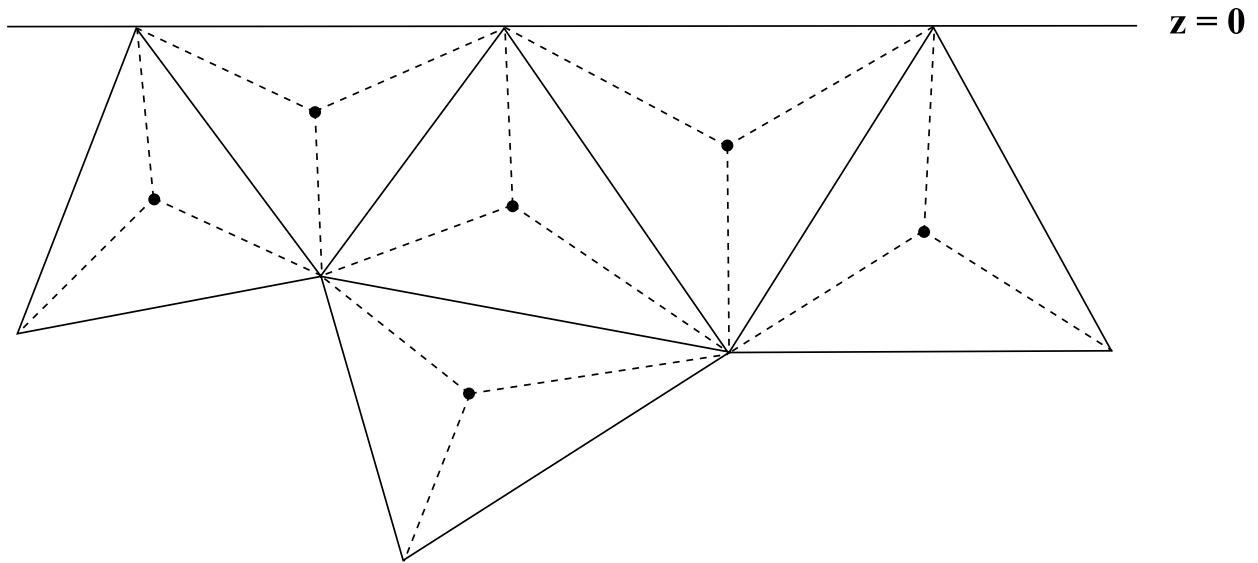


Figure 1: An example of the initial triangulation \mathcal{T}'_h (denoted by solid lines) and the subdivision of triangles of \mathcal{T}'_h by interior points (denoted by solid dots).

Chung et al. –

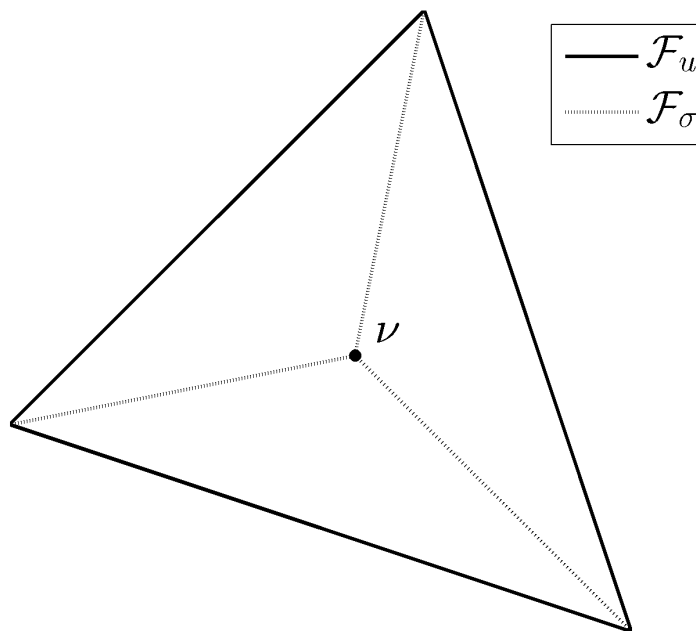


Figure 2: A first-type macro element $\mathcal{S}(\nu)$. **Chung et al.** –

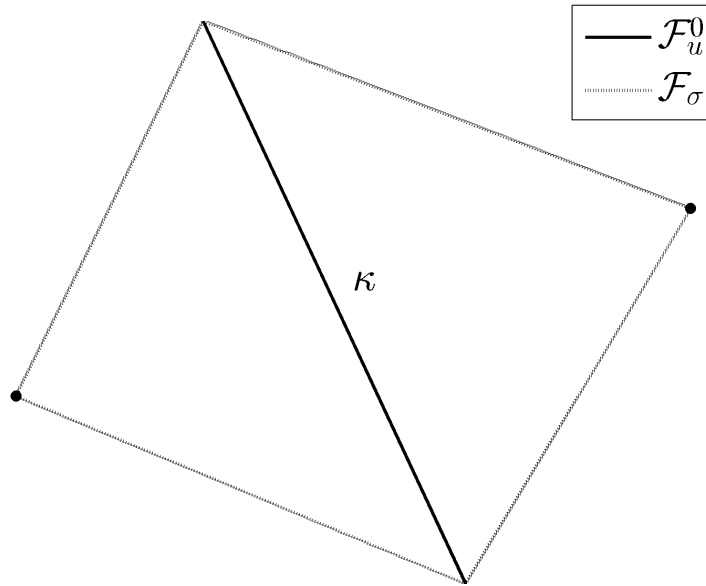


Figure 3: A second-type macro element $\mathcal{R}(\kappa)$. **Chung et al.** –

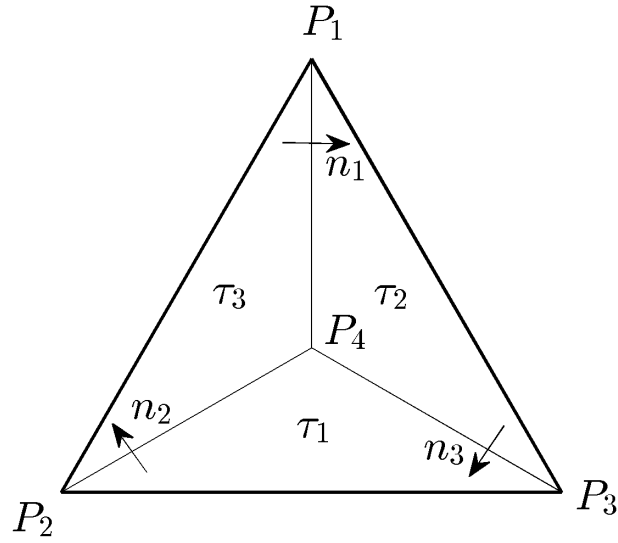


Figure 4: Notations for the construction of basis for W_h . **Chung et al.** –

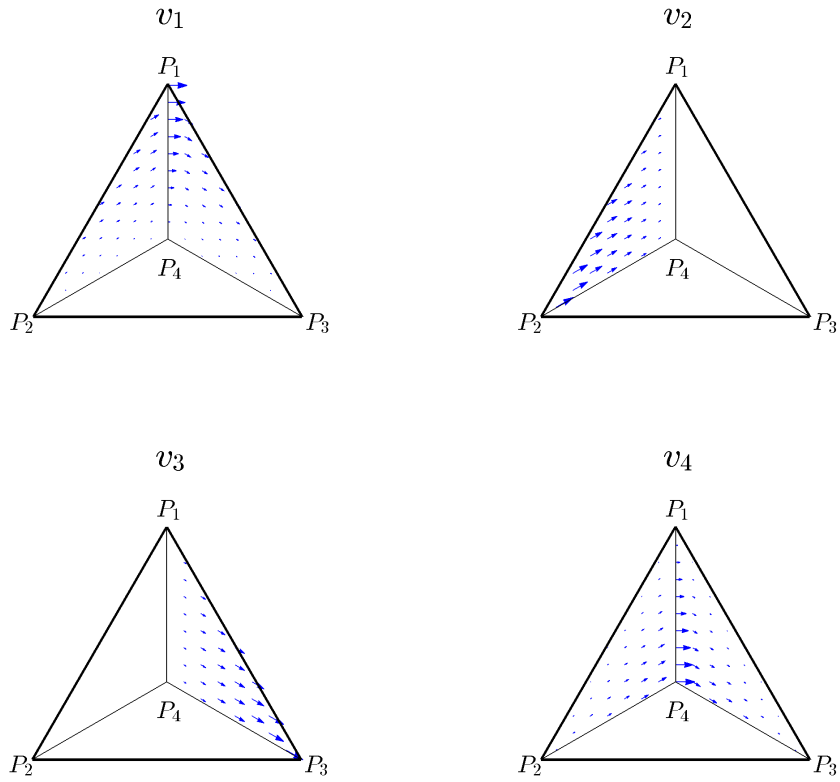


Figure 5: Plots of the first-type basis functions for W_h on $S(\nu)$ with $m = 1$. Chung et al. –

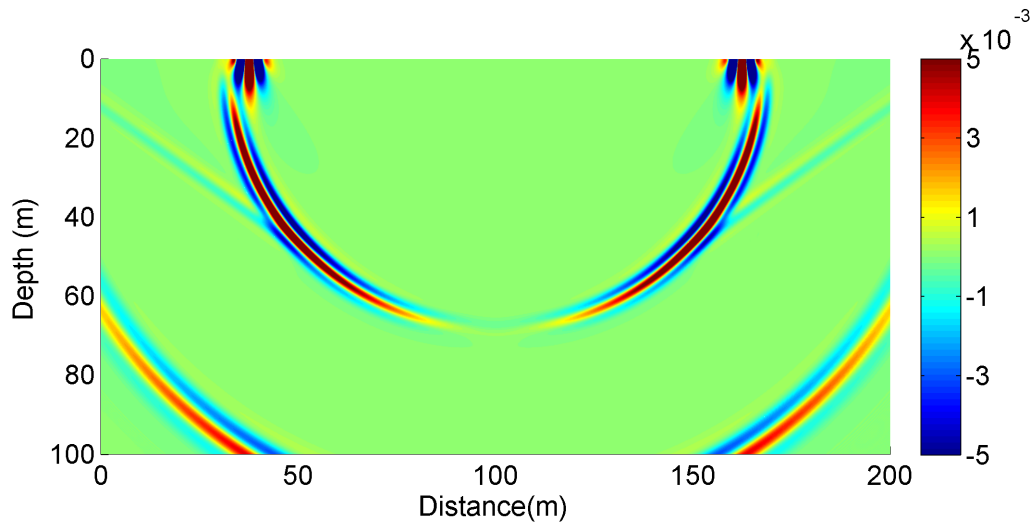


Figure 6: The snapshot for the vertical velocity u_2 at $t = 0.25s$ in example 1. **Chung et al.** –

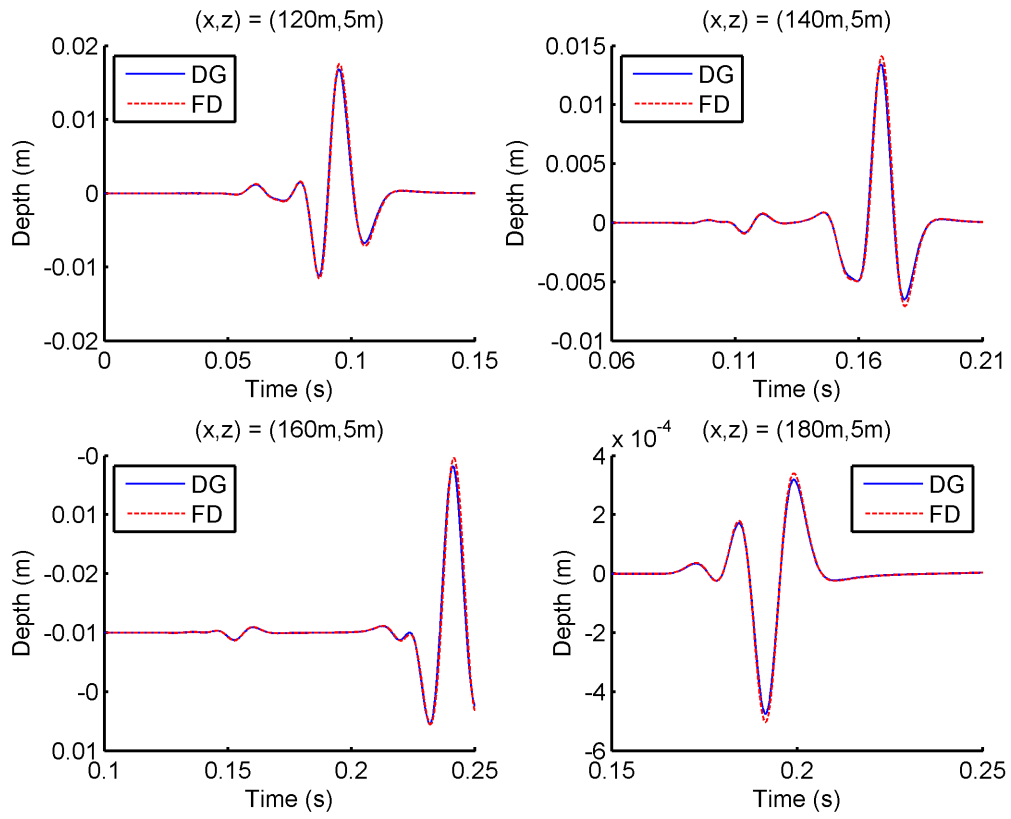


Figure 7: Comparison of our solution (DG) to a fourth-order finite different scheme (FD) at various observation points in example 1.

Chung et al. –

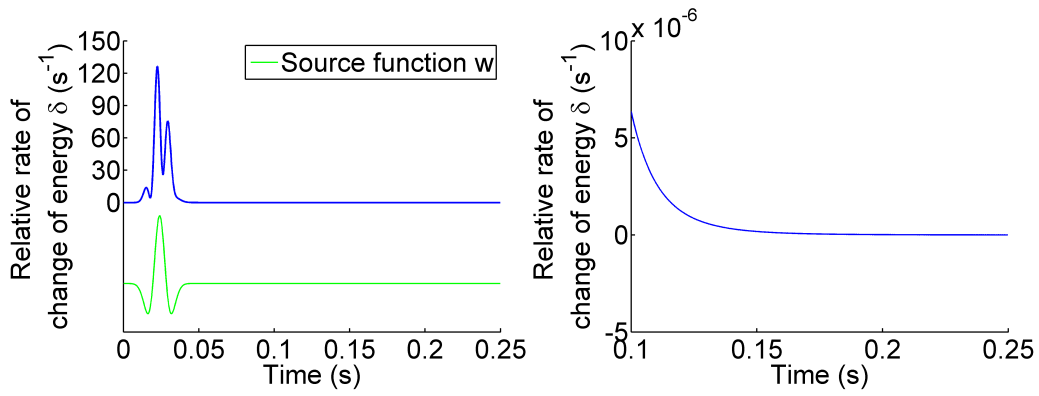


Figure 8: The relative rate of change of the energy function $E(t)$ in example 1. Note that the green line, which represents the source function, is not related to the y axis in the figure.

Chung et al. –

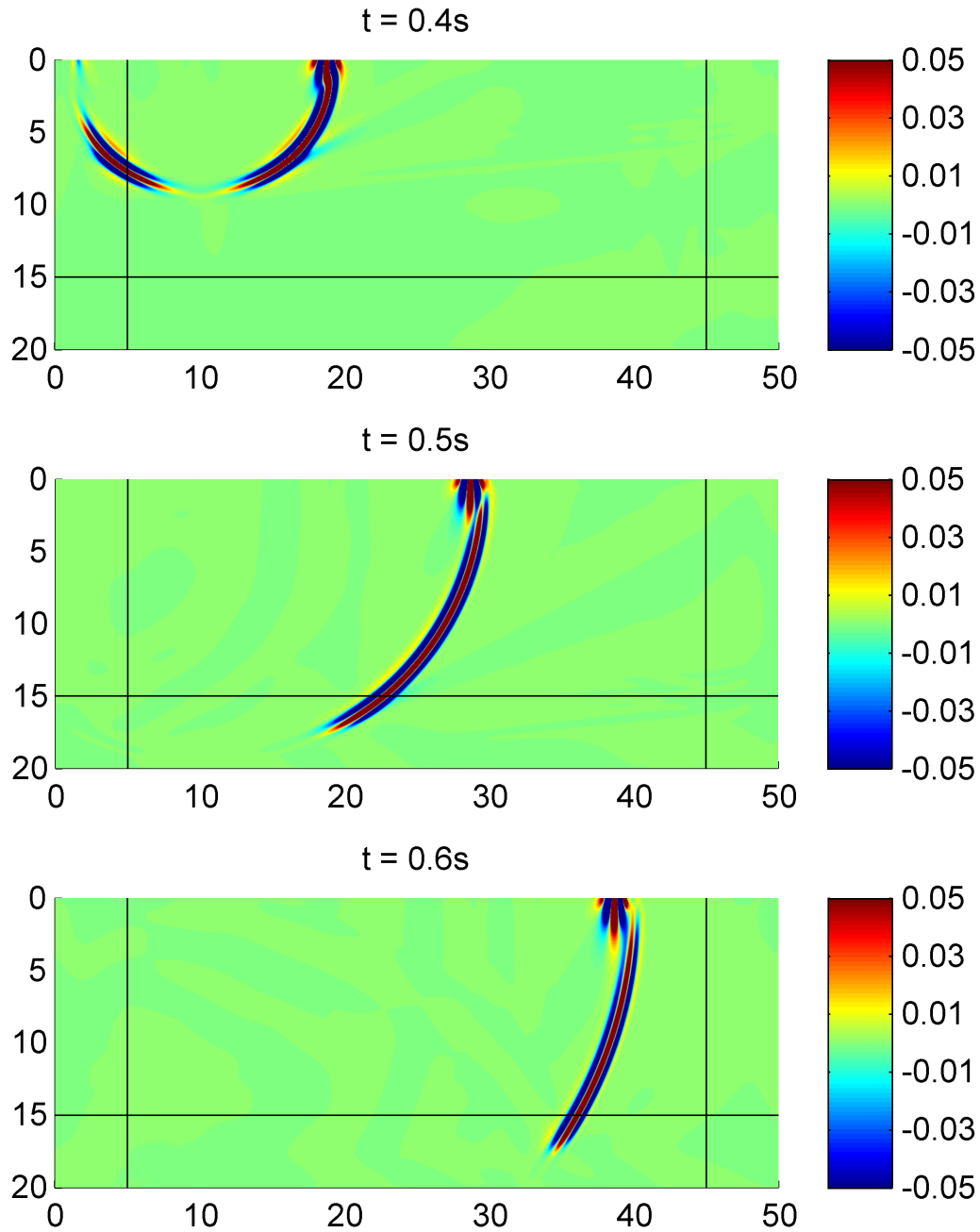


Figure 9: Snapshots for the vertical velocity u_2 in example 2. The black lines indicate the interface between the domain of interest and the MPMLs.

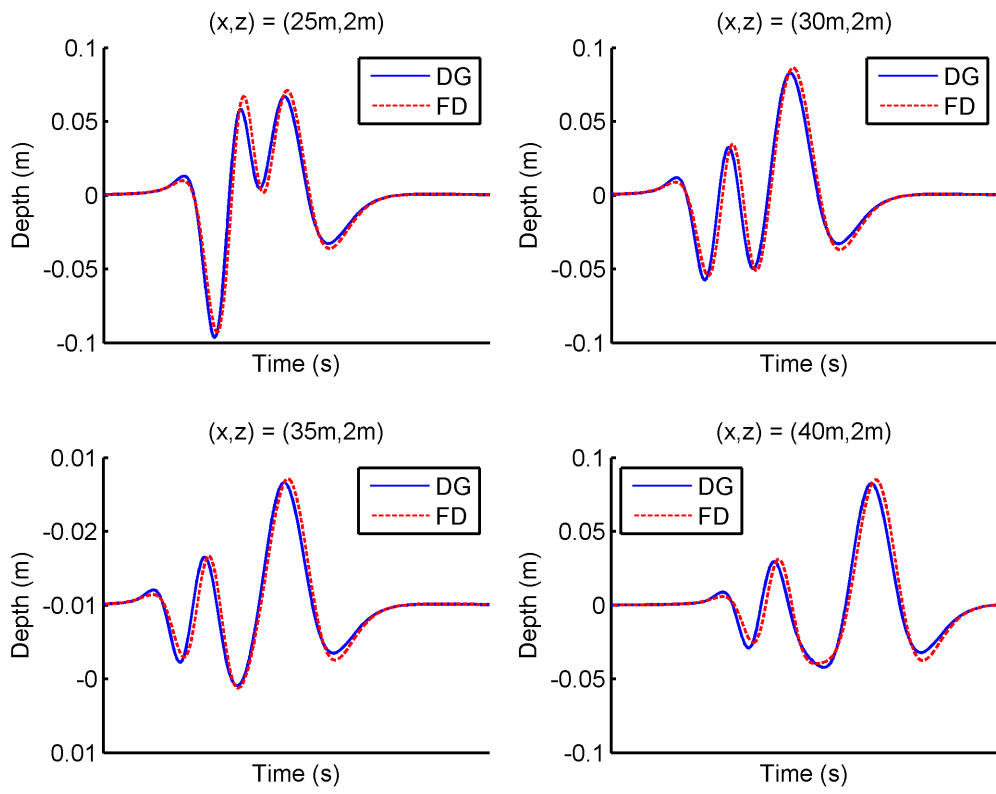


Figure 10: Comparison of our solution (DG) to a fourth-order finite difference scheme (FD) at various observation points in example 2.

Chung et al. –

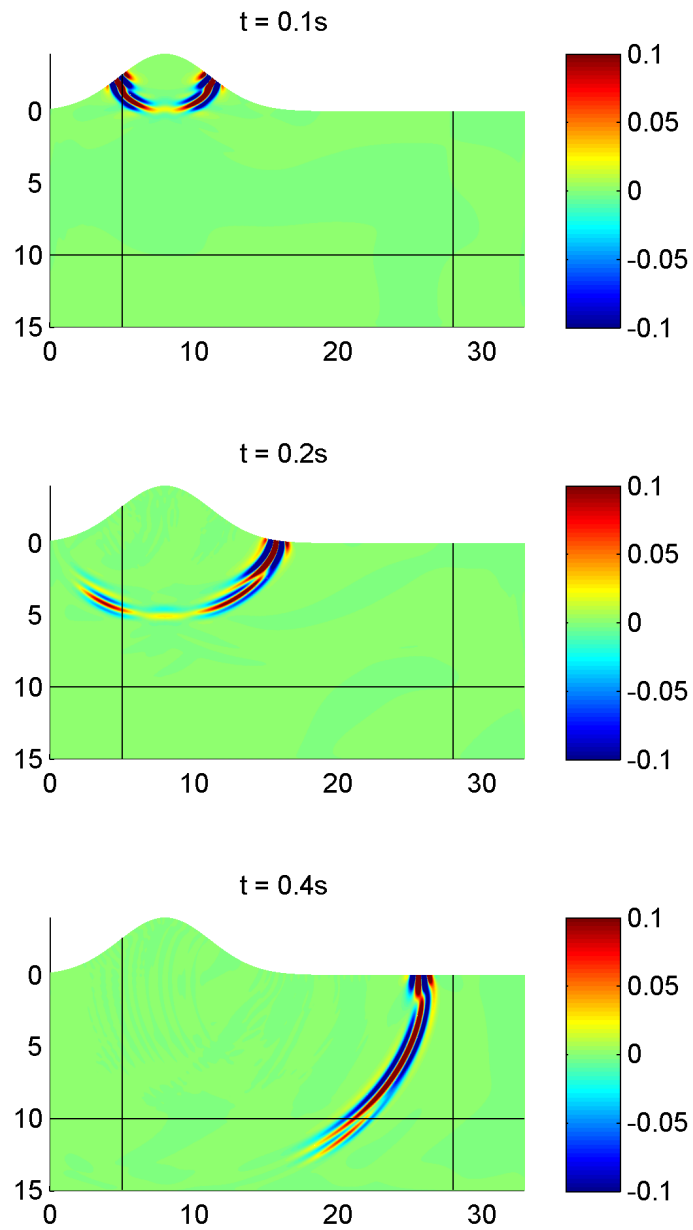


Figure 11: Snapshots for the vertical velocity u_2 in example 3. The black lines indicate the interface between the domain of interest and the MPMLs.

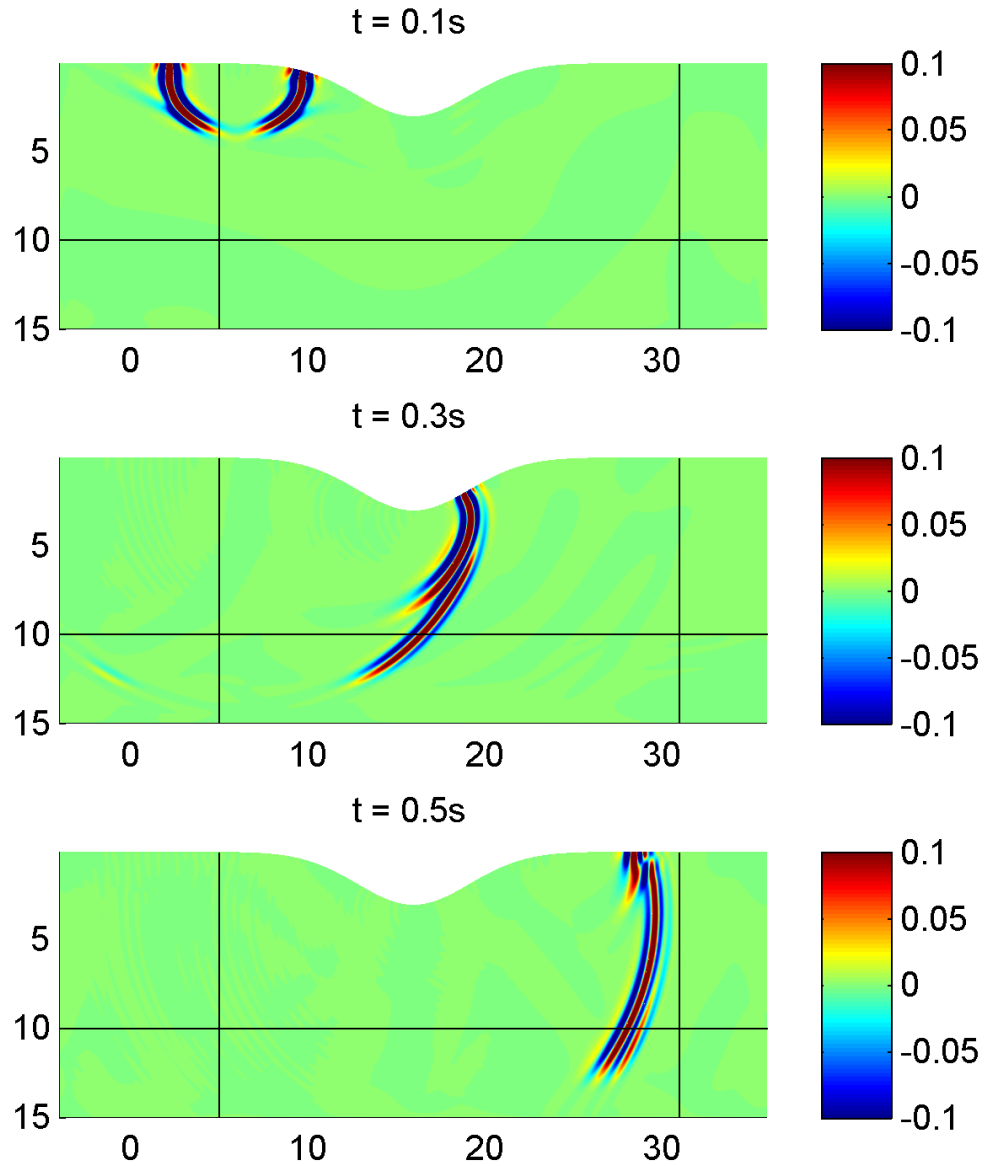


Figure 12: Snapshots for the vertical velocity u_2 in example 4. The black lines indicate the interface between the domain of interest and the MPMLs.

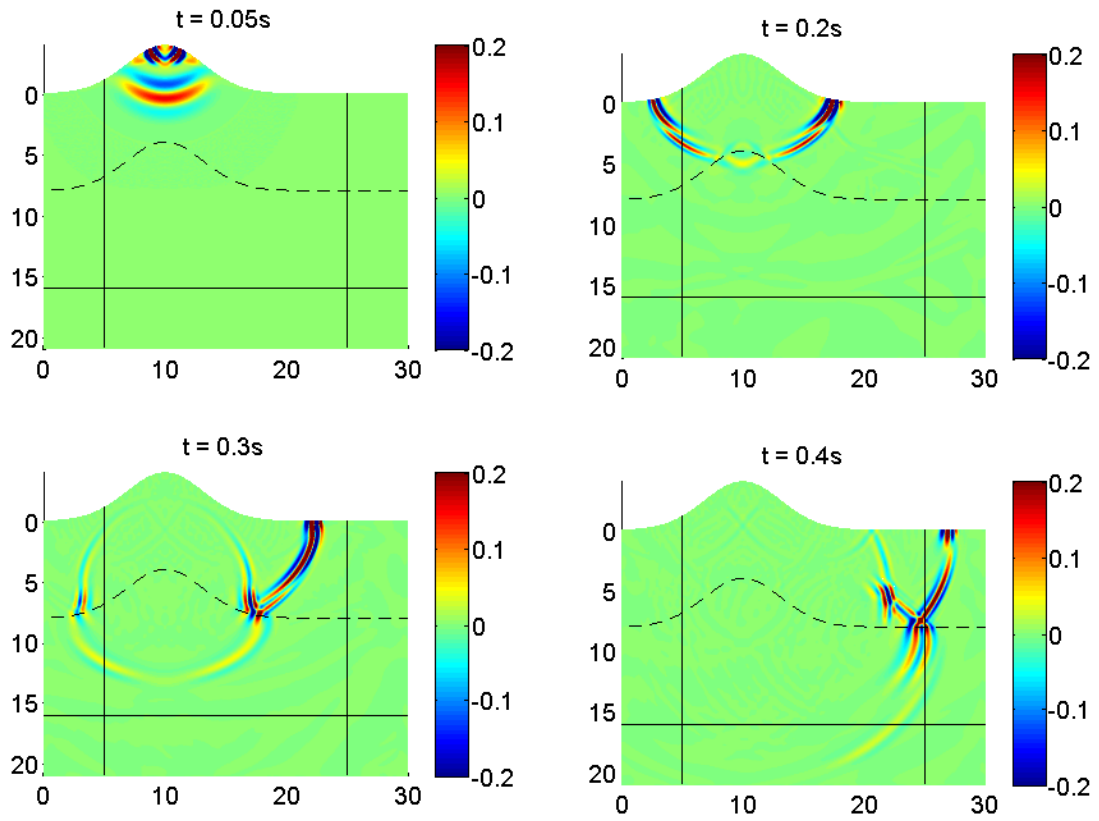


Figure 13: Snapshots for the vertical velocity u_2 in example 5. The black lines indicate the interface between the domain of interest and the MPMLs. The dotted lines indicate the interface between the two materials.

Chung et al. –